Saturation of destratifying and restratifying instabilities during down-front wind events: a case study in the Irminger Sea

F. W. Goldsworth[1,2], H. L. Johnson[3], D. P. Marshall[1], I. A. Le Bras[4]

[1]AOPP, Department of Physics, University of Oxford, Oxford, UK
[2]Oxford NERC Environmental Research DTP, Oxford, UK
[3]Deparment of Earth Science, University of Oxford, Oxford, UK
[4]Woods Hole Oceanographic Institution, Woods Hole, MA, USA

Key Points:

- Down-front wind events produce approximately 1.5 Sv of water mass transformation off the coast of Greenland between November and April.
- Mixing is induced by symmetric and gravitational instabilities.
- Baroclinic instabilities subsequently restratify the water column.

Corresponding author: F. W. Goldsworth, `fraser.goldsworth@physics.ox.ac.uk`

Abstract

Observations indicate that symmetric instability is active in the East Greenland Current during strong northerly wind events. Theoretical considerations suggest that baroclinic instability may also be enhanced during these events. An ensemble of idealised numerical ocean models, forced with northerly winds show that the short time-scale response (from two to four weeks) to the increased baroclinicity of the flow is the excitation of symmetric instability, which sets the potential vorticity of the flow to zero. The high latitude of the current means that the zero potential vorticity state has low stratification, and symmetric instability destratifies the water column. On longer time scales (greater than four weeks), baroclinic instability is excited and the associated slumping of isopycnals restratifies the water column. Eddy-resolving models that fail to resolve the submesoscale should consider using submesoscale parameterisations to prevent the formation of overly stratified frontal systems following down-front wind events.

The mixed layer in the current deepens at a rate proportional to the square root of the time-integrated wind stress. Peak water mass transformation rates vary linearly with the time-integrated wind stress. The duration of a wind event leads to a saturation of mixing rates which means increasing the peak wind stress in an event leads to no extra mixing. Using ERA5 reanalysis data we estimate that between 1.5 Sv and 1.8 Sv of East Greenland Coastal Current Waters are produced by mixing with lighter surface waters during wintertime by down-front wind events. Similar amounts of East Greenland-Irminger Current water are produced at a slower rate.

Plain Language Summary

Symmetric instability is a process that mixes waters at the surface of the ocean with denser waters below them. Observations show that in winter, when winds blow from the north, along the coast of Greenland, symmetric instability occurs; however, observations are limited which makes it difficult to understand the effect of the instability on the ocean currents in the region. We test the hypothesis that symmetric instability leads to the production of dense waters which are known to form in the region and contribute to the Atlantic Meridional Overturning Circulation, (or "ocean conveyor" (Broecker, 1991)). We find that symmetric instability doesn't lead directly to the formation of deep waters; instead it mixes lighter water with denser water which may subsequently form deep waters. A second type of instability, called baroclinic instability leads to the development of a fresh water "lid" which sits on top of the newly formed waters masses, isolating them from the atmosphere.

State of the art climate models don't resolve symmetric instability which means they may not get the density structure in the sub-polar North Atlantic correct, which could lead to errors in ocean heat transports which are important in determining the Earth's climate.

1 Introduction

The Irminger Sea is the region of the North Atlantic that sits between the East Coast of Greenland, the West Coast of Iceland and the Reykjanes Ridge. It has recently been revealed by OSNAP observations to be an important region in the formation of dense North Atlantic Deep Waters which make up the lower limb of the AMOC (Lozier et al., 2019). This finding came as a surprise to many, with most models suggesting deep water formation primarily occurs in the adjacent Labrador Sea (Hirschi et al., 2020). As such, there has been a renewed interest in processes that may enhance deep water formation in the Eastern Sub-polar North Atlantic Ocean (de Jong & de Steur, 2016; Josey et al., 2019; Le Bras et al., 2022).

One such process is symmetric instability, with observations indicating that it is excited in the East Greenland Current system during strong northerly wind events (Le Bras et al., 2022). The East Greenland Current system consists of two surface intensified western boundary currents within the Irminger Sea. They flow southwards along the east coast of Greenland, with the East Greenland Coastal Current on the landward side, and the East Greenland-Irminger Current sitting on the seaward side. The combined volume transport is around 18 Sv with peak speeds of around 20 $\mathrm{cm\,s^{-1}}$ found in the Irminger Current (Talley et al., 2011a, 2011b; Daniault et al., 2011; Le Bras et al., 2018). Symmetric instability within the current leads to the generation of a deep low potential vorticity layer 1.5 to 4 times deeper than the conventionally defined mixed layer (Le Bras et al., 2022; Taylor & Ferrari, 2010). Le Bras et al. (2022) hypothesised that the buoyancy fluxes associated with the excitement of symmetric instability may contribute to the formation of North Atlantic Deep Waters.

Symmetric instability occurs when there is an imbalance between a fluid parcel's inertia, and the Coriolis and buoyancy forces acting on it. It can be shown that this condition is equivalent to its Ertel potential vorticity having opposite sign to the vertical component of the planetary vorticity[1] (Ertel, 1942; Stone, 1966; Hoskins, 1974). When symmetric instability is excited, slantwise convection occurs. Slantwise convection is when overturning cells develop in a region of negative potential vorticity oriented almost parallel to isopycnals (Emanuel, 1994). The horizontal scale of the cells is typically set by the width of the negative potential vorticity region whereas the vertical scale is set by both the rate of turbulent mixing, which acts to erode small scale overturning motions, and the stratification, which prohibits the formation of tall overturning cells (Plougonven & Zeitlin, 2009).

For the East Greenland Current to become symmetrically unstable it must be injected with negative potential vorticity — during down-front wind events, this injection is provided by an Ekman buoyancy flux. Ekman driven symmetric instability occurs when potential vorticity is made negative by winds blowing along a geostrophically balanced current (Thomas & Lee, 2005). Consider a southwards flowing surface intensified current in the Northern Hemisphere. In order to balance the vertical shear, thermal wind balance requires the outcropping of dense waters in the East (figure 1). A northerly wind stress blowing along the current will induce a westwards Ekman transport (figure 2), which will act to steepen the isopycnals (Allen & Newberger, 1996). For a current in thermal wind balance, potential vorticity is given by

$$Q = \left(f + \frac{\partial V}{\partial x}\right)\frac{\partial b}{\partial z} - \frac{1}{f}\left(\frac{\partial b}{\partial x}\right)^2. \tag{1}$$

If the stratification is stable, and the planetary vorticity dominates over relative vorticity, as is typical when more than a few degrees away from the equator, then the first term in the equation will have the same sign as f. The quantity $(\partial_x b)^2$, however, is positive semi-definite, so the second term will always act to make the potential vorticity more anomalous (Haine & Marshall, 1998) — that is it will make the flow less stable to symmetric instability. As the isopycnals steepen the $\partial_z b$ term decreases and the $\partial_x b$ term increases so that eventually, if the isopycnals become sufficiently steep, the potential vorticity can become negative, rendering the flow unstable to symmetric instability (Thomas & Lee, 2005).

[1] Note that in this work we will use the classical definition of symmetric instability (Hoskins, 1974) rather than the energetic definition of Thomas and Lee (2005). For more information see chapter 2 of F. W. Goldsworth (2022). Under the classical definition both inertial and gravitational instabilities *are* also symmetric instabilities, whereas, under the energetic definition they are distinct.

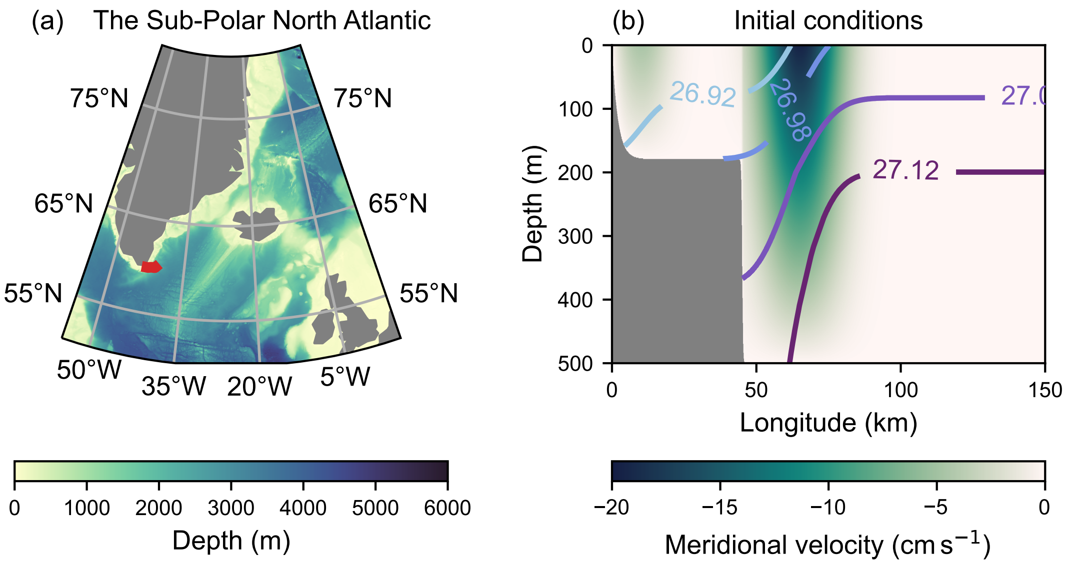

Figure 1. (a) The bathymetry of the Sub-Polar North Atlantic (GEBCO Compilation Group, 2020). Red line indicates the OSNAP section which the initial conditions and wind forcing used in our models are based on. (b) The density and velocity structure used to initialise the idealised models.

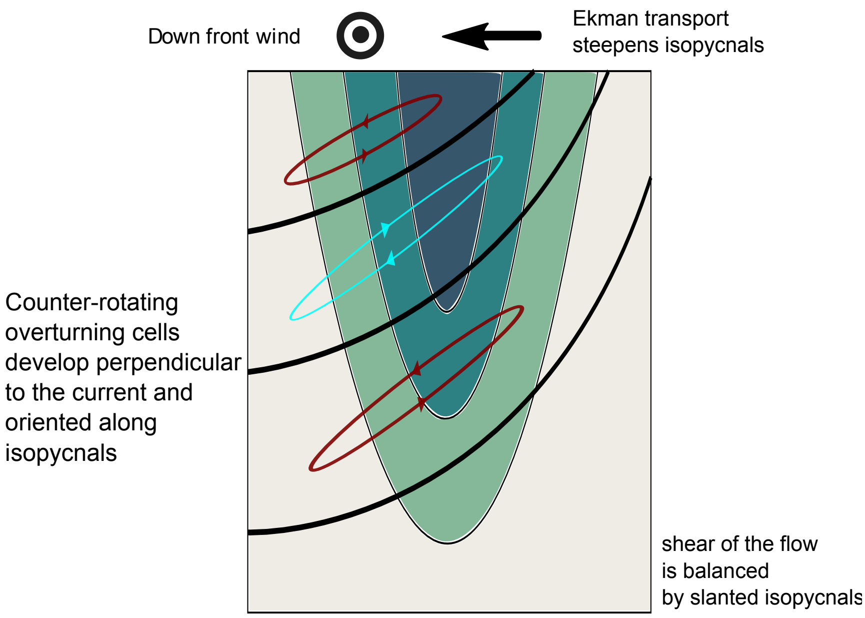

Figure 2. Schematic showing generation of slantwise overturning cells during a down-front wind event. Northerly winds blow along the current leading to a westward Ekman transport of outcropping isopycnals. This in turn reduces potential vorticity leading to the excitement of symmetric instability in regions where the potential vorticity is negative. Symmetric instability is characterised by stacked, counter-rotating overturning cells which orient themselves almost parallel to isopycnals.

The idea that Ekman induced symmetric instability is an important mechanism in the formation of deep waters in the Sub-polar North Atlantic is not a new one. Straneo et al. (2002) found that wind-driven Ekman buoyancy fluxes over the Labrador Sea can be around a third of the size of the air-sea buoyancy flux, and concluded that symmetric instability should be taken into account when modelling deep water formation in the region. More recently Clément et al. (2023) found that the restratifying effect of symmetric instability and mixed layer eddies is responsible for the cessation of deep convection in the Labrador Sea. Indeed, that symmetric instability can both restratify and destratify further motivates this study. Ongoing modelling work is being carried out by Shu (2023) investigating symmetric instability and baroclinic instabilities in the region. Similarly to Clément et al. (2023) they see the formation of mixed layer eddies; however they also see symmetric instability destratifying the mixed layer.

Spall and Thomas (2016) investigate the effect of down-front winds in an idealised model of a buoyant coastal plume, similar to the East Greenland Current. They integrate both two-dimensional and three-dimensional hydrostatic models, with a horizontal grid spacing of 500 m and a vertical grid spacing of 1 m. They force their models with a uniform meridional wind stress which is ramped up over seven days and then held constant for the remaining thirteen days of model integration. In their models, they observe symmetric instability which sets the potential vorticity to near zero, alongside baroclinic instability. These two processes act together to produce water mass transformations, with baroclinic instability greatly enhancing the transformation rates.

Other field and modelling campaigns have investigated the role of Ekman driven symmetric instability in various boundary current and frontal systems. Thomas et al. (2013) observed symmetric instability in the Gulf Stream under down-front winds and found a competition between destratification of the mixed layer by convection and restratification resulting from symmetric instabilities. Similar effects have been observed by D'Asaro et al. (2011) in the Kuroshio, and conditions conducive to the excitement of Ekman driven symmetric instability have been observed in the Antarctic Circumpolar Current (Taylor et al., 2018).

The observations of Le Bras et al. (2022), taken in the East Greenland Current region, raise questions about how much water mass transformation is driven by down-front wind events, and whether these highly seasonal events could be a source of AMOC variability. These questions are incredibly difficult to answer with sparse observations, and so here we will use idealised models to tackle them. Our results could also be used to evaluate parameterisations for mixing induced by down-front wind events (although we will not attempt to do this here). The work of Spall and Thomas (2016) lays the foundations for addressing the above questions; however, their study design means it is only able to partially answer them. Their hydrostatic models are too coarse to provide a truly reliable estimate of the mixing induced by symmetric instability. A non-hydrostatic model with a higher resolution is required to resolve the secondary shear instabilities which are known to be important in generating mixing (Taylor & Ferrari, 2009).

In the model simulations of Spall and Thomas (2016), the wind stress is held constant after the first seven days of model integration. This means both potential vorticity and buoyancy are constantly being extracted from the flow, and the models will only equilibriate to a pseudo-steady state in which instability will constantly be excited. Therefore, estimates of mixing at later times in their integrations may be either overestimates or underestimates, depending upon whether the preconditioning by the wind stress at earlier times enhances or suppresses subsequent mixing. To estimate the effect of a wind event on mixing, we must model it as just that — an isolated event, with a wind stress which is ramped up and down to some characteristic value over a characteristic period of time.

In this work we address:

Run	τ_0 ($\mathrm{N\,m^{-2}}$)	δ_t (days)	ΔX (m)	Pressure	Dimensions
Standard 2D	0.5	2.5	25	NH	2D
Standard 3D	0.5	2.5	200	H	3D
Coarse 2D	0.5	2.5	200	H	2D
Ensemble	0 — 0.75	0 — 5	25	NH	2D

Table 1. Table showing parameters used in the different model integrations. τ_0 = maximum down-front wind stress. δ_t = wind event duration. ΔX = model resolution. NH = non-hydrostatic. H = hydrostatic.

1. how symmetric and baroclinic instabilities alter the mean structure of the East Greenland Current following down-front wind events;
2. the role of baroclinic and symmetric instabilities in producing diapycnal mixing during down-front wind events;
3. approaches to parameterising symmetric instability in coarse resolution models that fail to resolve the process.

Although this work focuses on the East Greenland Current, the findings will be applicable to other boundary current systems which are subject to down-front winds.

In section 2 we describe the suite of idealised models that underpin this study. In section 3 we examine the effects of symmetric and baroclinic instabilities on the structure of the (modelled) East Greenland Current following down-front wind events. In section 4 we take a more quantitative look at the depth of the low potential vorticity layer and water mass transformation rates, before examining the implications for numerical climate models. Finally, in section 6 we summarise our results and make concluding remarks.

2 The models

We integrate an ensemble of idealised models of the East Greenland current based on two different configurations of the MITgcm (Marshall et al., 1997; Campin et al., 2022). The first configuration is a non-hydrostatic two-dimensional model that is symmetric (periodic) in the along-stream direction. The domain is 150 km wide in the horizontal (across-stream) direction and 500 m deep. The horizontal and vertical grid spacings are set to 25 m and 1 m, respectively. The resolution was chosen to be high enough that the Richardson number is sufficiently small for Kelvin-Helmholtz instabilities to be resolved, as Kelvin-Helmholtz instabilities are known to be important for obtaining reliable estimates of diapycnal mixing rates (Griffiths, 2003; Yankovsky & Legg, 2019). The time step is set to 2 seconds and the model is integrated for a total of 21 days.

This first configuration allows us to probe the fine-scale dynamics that occur during down-front wind events; however, the two-dimensional nature of the models prohibits the development of baroclinic instability which grows in the along stream direction (Stone, 1966). Given the high baroclinicity of the current system, it is plausible that baroclinic instability will have a material effect on the dynamics. In order to resolve baroclinic instability we require a three-dimensional model. As such we also integrate a second set of model configurations which compromise on resolution but can be run in either a two-dimensional or three-dimensional setup.

The second configuration is hydrostatic and has a horizontal resolution of 200 m. In the three-dimensional setup the model domain has a meridional extent of 50 km, with periodic meridional boundaries. The time step is set to 4 seconds. The model is integrated for a total of 84 days. The model setup is otherwise identical to the non-hydrostatic configuration. A summary of the model integrations is shown in table 1.

Both configurations are sited on an f-plane with f set to 1.26×10^{-4} s^{-1}, corresponding to a latitude of 60°N. At the surface, a rigid lid boundary condition is employed, with the lateral and bottom boundaries set to be free-slip. The model has sloping bathymetry, which can be seen in figure 1b. The model is initialised in thermal wind balance, with the velocity field and density profiles also shown in figure 1b. Both of these fields are based on observations from the OSNAP array (Le Bras et al., 2022).

A linear equation of state is used, with a reference density of 1,027 kg m^{-3}, a thermal expansion coefficient of 2×10^{-4} K^{-1}, and constant salinity. The thermal diffusion coefficient is set to 1×10^{-5} m^2 s^{-1}. A second order-moment Prather advection scheme with a flux limiter is employed (Prather, 1986). Momentum dissipation is provided by an adaptive biharmonic lateral Smagorinsky viscosity and a vertical Laplacian viscosity of 4×10^{-4} m^2 s^{-1} (Smagorinsky, 1963; Griffies & Hallberg, 2000). The biharmonic viscosity is chosen to ensure dissipation occurs as close to the grid-scale as possible.

The models are forced using a time-varying, along-stream wind stress. The stress is spatially uniform and temporally Gaussian, taking the form

$$\tau_y = \tau_0 e^{-(t-t_{mid})^2/2\delta_t^2}\ , \tag{2}$$

where τ_0 is the maximum wind stress, t_{mid} is the time at which the wind stress peaks and δ_t is the duration of the wind event. We integrate the non-hydrostatic configuration using ten different values of τ_0 ranging linearly from 0 N m^{-2} to -0.75 N m^{-2} and four different values of δ_t ranging linearly from 1.25 days to 5 days, giving 37 different ensemble members[2]. In all integrations t_{mid} is set to 10.5 days.

We define the set of standard integrations as those in which $\tau_0 = -0.5$ N m^{-2} and $\delta_t = 2.5$ days. This set consists of a hydrostatic and non-hydrostatic two-dimensional integration, and a non-hydrostatic three-dimensional integration. Each of these models is integrated for 84 days.

In some of the model fields plotted here, thin horizontal and vertical lines are present. Investigation of their locations suggests they are a result of sharp "lego-like" bathymetry in the the models. As far as we are aware, the features only come to prominence in fields involving derivatives and they have no effect on the large scale dynamics.

3 Instabilities and the background flow

3.1 Symmetric instability

We first investigate the response to down-front winds in the standard two-dimensional model setup, in which symmetric instability and Kelvin Helmholtz instabilities may be excited, but in which baroclinic instability is not able to develop.

Examining the isopycnals plotted in figure 3a, we see how after 1 week of down-front wind forcing there is an Ekman transport of surface waters towards the shelf, leading to a steepening of isopycnal surfaces. In panels (a) and (d) we see how both the potential vorticity and stratification are made negative near the surface, rendering the flow unstable to both symmetric and gravitational instabilities. Figure 4 shows the fraction of wet grid points susceptible to each of these instabilities as a function of depth and time

[2] Note that when the wind stress is zero it doesn't matter how long the wind event is meaning there are only $40 - 3 = 37$ unique ensemble members.

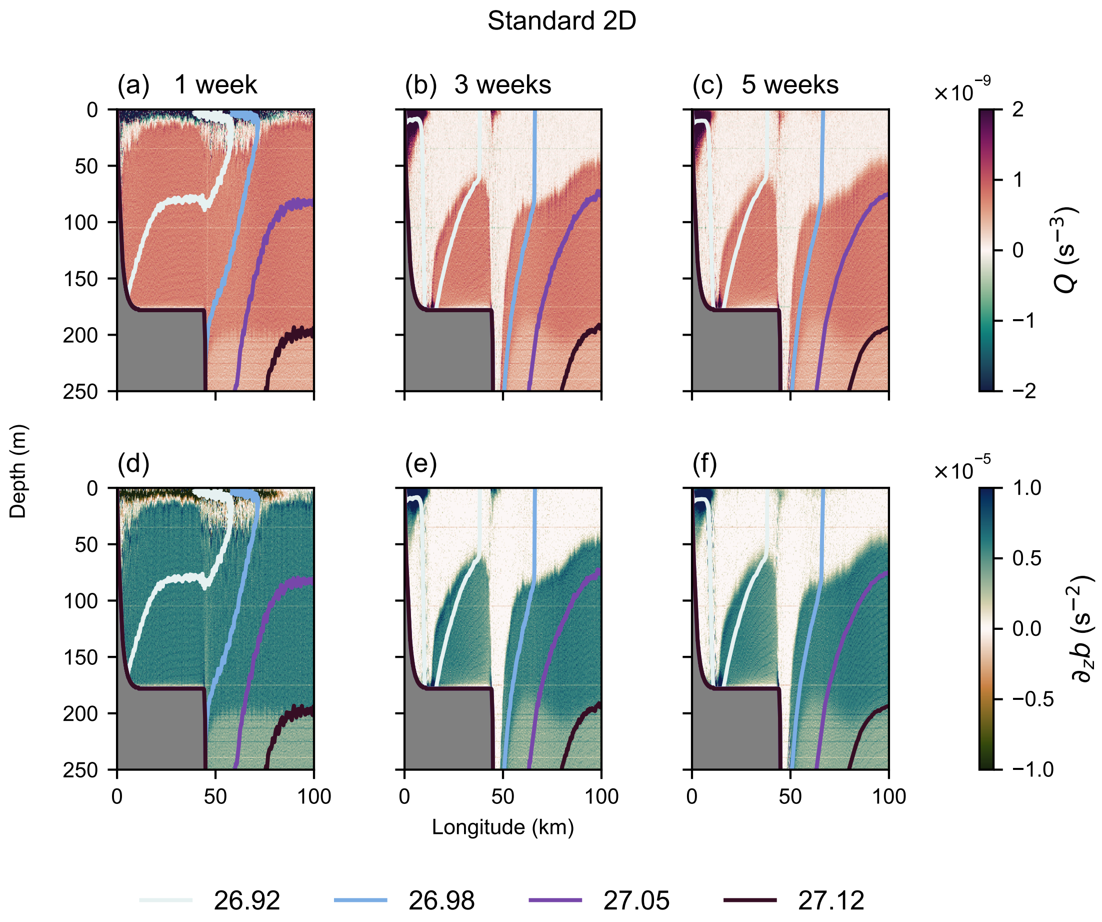

Figure 3. (a-c) Potential vorticity and (d-f) Stratification in the standard non-hydrostatic two-dimensional model integration. Overlain contours show isopycnals.

in the integration. Note that gravitational instability is dominant in the surface whereas symmetric instability dominates below around 15 metres. The fraction of grid points susceptible to symmetric instability remains large well after the wind forcing has subsided (i.e. past 21 days). Figure 3c suggests this is largely due to patches of near zero but negative potential vorticity. Although these regions may be susceptible to symmetric instability in principle, their potential vorticity is so close to zero that they are essentially in a state of marginal stability. The spatial structure of potential vorticity, stratification and density (as shown in figure 3) is very similar after three and five weeks, further supporting the hypothesis that symmetric instability is largely inactive during the time period following the wind event.

In panels (b) and (e) of figure 3 we see a deeply penetrating low potential vorticity layer, which has incredibly low stratification. The low stratification of this low potential vorticity layer makes distinguishing it from the conventionally defined convectively mixed layer difficult. The low potential vorticity layer we see here is deeper on the anticyclonic (shore-ward) flanks of the currents — an effect seen in observations too (Le Bras et al., 2022). It arises as regions of anticyclonic relative vorticity are less stable to symmetric instability: note that this deepening is not a bathymetric effect.

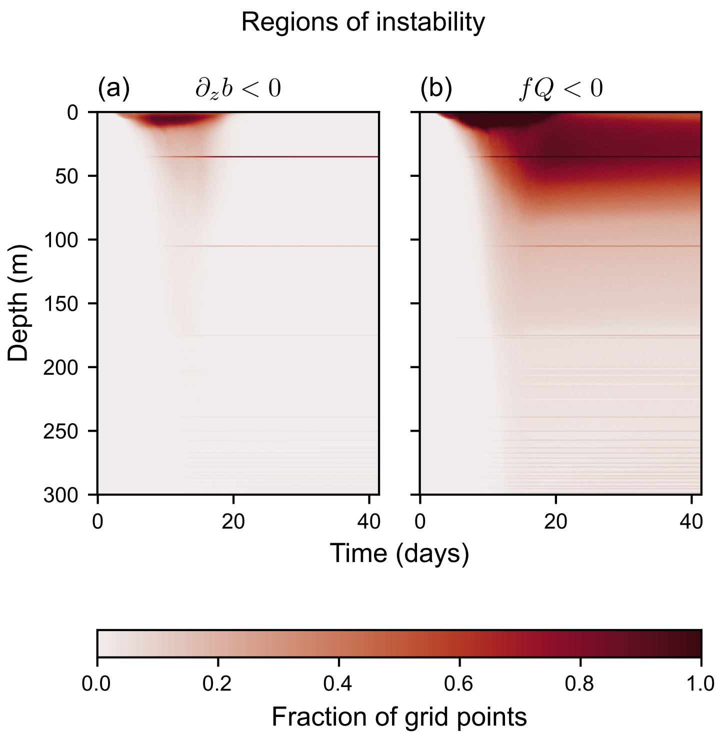

Figure 4. Fraction of grid cells susceptible to (a) gravitational instability and (b) symmetric instability as a function of depth and time in the standard non-hydrostatic two-dimensional model integration. Grid cells are taken to be susceptible to gravitational instability if $\partial_z b < 0$ and susceptible to symmetric instability if $fQ < 0$.

That the instability sets the vertical stratification to zero contrasts with studies of the Kuroshio and Gulf Stream, where it is found that the water column is restratified following the excitement of symmetric instability (D'Asaro et al., 2011; Thomas et al., 2013); however, the finding is consistent with observations from the Sub-polar North Atlantic (Le Bras et al., 2022) and the theory of Haine and Marshall (1998). We hypothesise that these differences stem from differences in planetary vorticity at high and mid latitudes — large planetary vorticity at high latitudes means that a zero potential vorticity state *must* have low stratification too. As we will shortly see in section 3.2 the absence of baroclinic instability in our two-dimensional models also leads to reduced stratification in regions where symmetric instability has occurred. Furthermore, our model resolution is high enough to resolve Kelvin Helmholtz billows at interfaces between overturning cells. These billows can be susceptible to gravitational instability, further contributing to the low stratification when our results are compared to coarser modelling studies (see for example figure S2 in the supplementary information which shows the stratification in the coarse two-dimensional model integration).

3.2 Baroclinic instability

The isopycnal structure following the excitement of symmetric instability (as seen in figure 3f) is highly baroclinic, especially in the surface 100 m. The steeply slanted isopycnals, although stable to symmetric instability, are unstable to baroclinic instability. Baroclinic modes grow in the along stream direction, however, meaning that they will not be resolved in our two-dimensional models with along stream symmetry. Because of this we will now examine output from the standard three-dimensional model run at a resolution of 200 m (standard 3D).

To ensure the resolution of this model is sufficient to capture the dynamics we are interested in, we also integrated a two-dimensional version of the model at the same resolution (coarse 2D) and compared its output with that of the finer non-hydrostatic reference simulation (standard 2D). We found that key fields such as potential vorticity and stratification are qualitatively similar and water mass transformation rates also look broadly similar (for more details see the supplementary information and figures 6 & 8.)

In figure 5 we show meridionally averaged potential vorticity and stratification in the standard three-dimensional model integration. At early times (figure 5a & d), these look very similar to the standard two-dimensional integration (figure 3a & d), with the generation of negative potential vorticity and unstable stratification towards the surface. At three weeks, however, the low potential vorticity layer appears more diffuse and we see signs of restratification and the slumping of isopycnals at the surface, concentrated in the eastern part of the domain (figure 5b & e). There is also restratification in the western part of the domain concentrated at the base of the inner shelf. Given the accompanying isopycnal slumping and the absence of the restratification in the two-dimensional models, we conclude that this is the effect of baroclinic instability. After five weeks, the stratification at the surface in the eastern part of the domain has increased further, resulting in a highly stratified "lid" on top of the low potential vorticity waters below. Furthermore the potential vorticity in the low potential vorticity layer is increased, a result of baroclinic eddies fluxing potential vorticity laterally and eroding potential vorticity gradients.

3.3 A hierarchy of instabilities

Other studies have found that baroclinic instability is more efficient at removing negative potential vorticity injected by Ekman buoyancy fluxes than symmetric instability (e.g. Haine & Marshall, 1998; Spall & Thomas, 2016). Our results do not contradict these previous works. In these studies, the authors force a front with constant winds in which a pseudo-steady state can be reached. In this steady state Ekman buoyancy

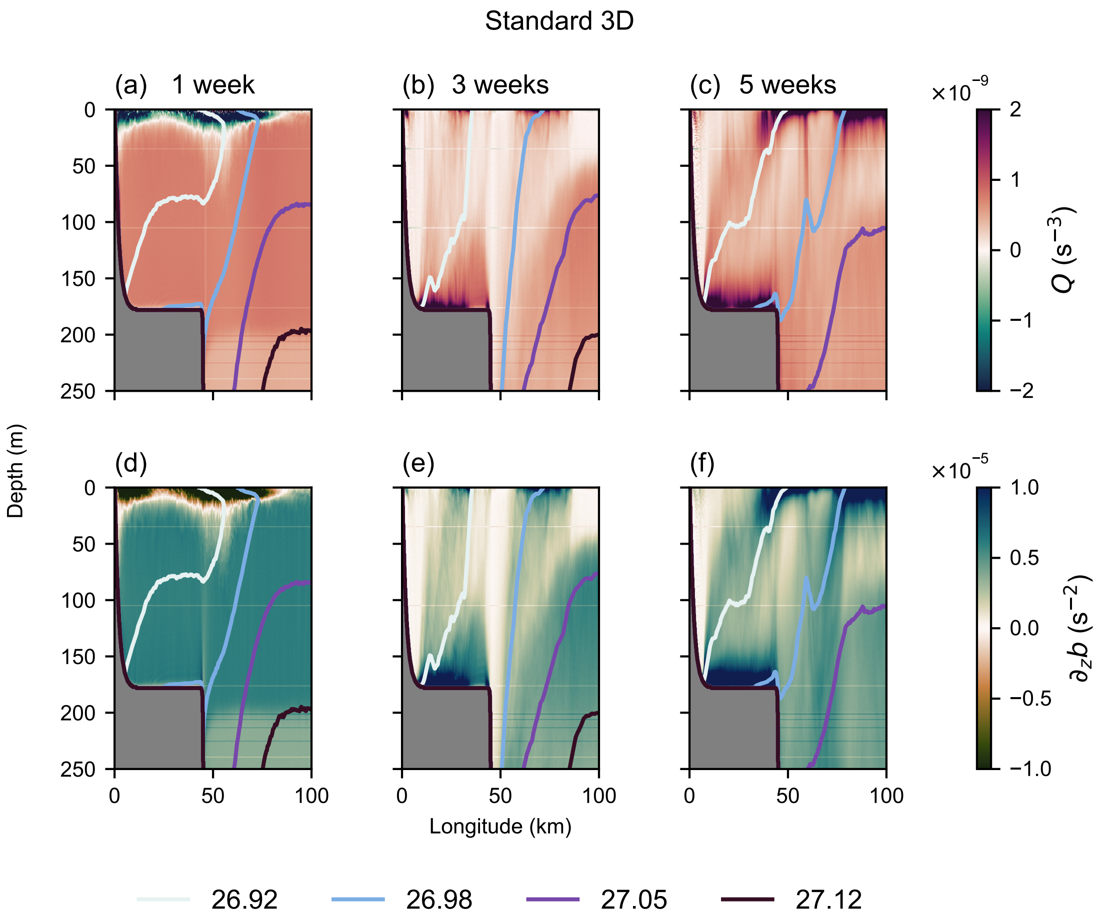

Figure 5. Evolution of meridionally averaged (a-c) potential vorticity and (d-f) stratification in the standard hydrostatic three-dimensional model integration. Overlain contours show isopycnals. Columns correspond to the quantities after 1 week, 3 weeks and 5 weeks.

fluxes are balanced by eddy fluxes. These eddies grow slowly over timescales given by the inverse of the Eady growth rate. During the initial stages of wind events when the flow is highly baroclinic, there may be other faster growing processes which are capable of steadying the system. Indeed, when the flow is highly baroclinic, symmetric instability can have a larger growth rate than that of baroclinic instability (Stone, 1966).

In our model simulations, we subject currents to wind stresses that are ramped up and back down again. Compared to the Eady growth rate, however, this ramping up and down behaves more like an impulse forcing which steepens the isopycnals faster than the steepening can be counteracted by any of baroclinic, symmetric or gravitational instability. On the shortest time scales (less than around two weeks) gravitational instability is excited in regions where the isopycnal tilt exceeds 90°. On intermediate time scales (from two weeks to four weeks) symmetric instability is excited in regions with negative potential vorticity. This typically corresponds to isopycnal tilts in excess of around 5°. And, finally, on long timescales (after around four weeks) baroclinic instability will be excited. The transition from gravitational to symmetric instability and symmetric to baroclinic instabilities will occur when their growth rates are of similar orders of magnitude for the isopycnal structure of the time. The transition from gravitational to symmetric instability can be expected to occur for a Richardson number of around one (Thomas et al., 2013), and for symmetric to baroclinic instability this corresponds to a Richardson number of 0.95 (Stone, 1966). In reality, all three instabilities will be growing concurrently and interacting with each other (Stamper & Taylor, 2017); however, thinking in terms of a hierarchy of instabilities is a useful abstraction.

4 Diapycnal mixing

The observations of Le Bras et al. (2022) and the results shown here in figure 3 suggest that the excitement of symmetric instability may be a mechanism by which dense waters, such as North Atlantic Deep Waters, can be formed. It is difficult to quantify the diapycnal mixing that follows down-front wind events from the moored observations of Le Bras et al. (2022), so here we use our model ensemble to investigate the dependence of the low potential vorticity layer depth, and water mass transformation patterns, on the parameters of the down-front wind event.

4.1 Mixing depth

Taylor and Ferrari (2010) propose a scaling for the depth of the low potential vorticity layer generated during down-front wind events. Assuming the only forcing comes from winds and that the initial depth of the low potential vorticity layer is zero, the scaling can be summarised as

$$\frac{\mathrm{d}H^2}{\mathrm{d}t} \propto B_{wind} \tag{3}$$

where H is the depth of the low potential vorticity layer and B_{wind} is the Ekman buoyancy flux induced by the down-front winds, and is given by

$$B_{wind} = -\frac{\tau_y \partial_x b}{\rho_0 f}\,. \tag{4}$$

Integrating equation 3 under the assumption that $\partial_x b$ is approximately constant, we find that

$$H(t = t_{end}) \propto \tau_{int}^{1/2}\,, \tag{5}$$

where τ_{int} is the temporally integrated wind stress. As noted already, the low potential vorticity layer in our models, due to its low stratification, is almost indistinguishable from

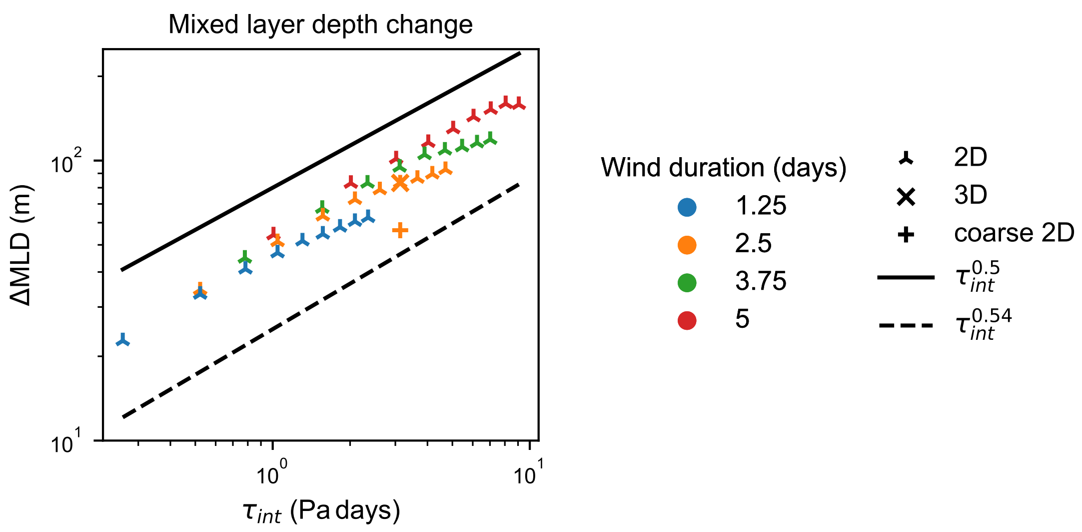

Figure 6. Spatially averaged change in mixed layer depth between day 21 and day 0, a a function of integrated wind stress. Both horizontal and vertical axes are logarithmic. Triagonal markers correspond to integrations from the 2D ensemble, the cross the standard 3D, and the plus the coarse 2D integrations. Colours show the duration of the wind event. The solid line shows the mixed layer depth scaling predicted by theory and the dashed line the scaling found across the 2D ensemble members.

the mixed layer. If we assume the change in mixed layer depth is a result of the expansion of the low potential vorticity layer we would expect changes in mixed layer depth to scale with the square root of the integrated wind stress.

We define the mixed layer depth as the depth at which density changes by 0.05 kg m^{-3} relative to the surface density. In figure 6 we show the change in mixed layer depth plotted against integrated wind stress for each member of our ensemble (note both axes are logarithmic). Performing a least squares regression on the ensemble data and using a t-test to estimate the confidence intervals, we find that the change in mixed layer depth scales with τ_{int} to the power of 0.54, with a 95% confidence interval of 0.49 to 0.58. This is remarkably consistent with the value of 0.5 predicted by idealised theory. Lines showing the 0.5 and 0.54 power laws are also shown in figure 6a. Note how, for a given wind duration, the change in mixed layer depth starts to saturate as the wind strength is increased. This saturation suggests that the amount of mixing may be limited by the duration of the wind event. We can understand why this occurs as follows: if we relax the condition of $\partial_x b$ being constant, integrating equations 3 & 4 by parts we find that

$$H^2(t) \propto \left(\tau_{int}(t)\partial_x b(t) - \int_{t'=t_0}^{t} \tau_{int}(t') \frac{\partial^2 b}{\partial x \partial t'} \mathrm{d}t' \, , \right) \tag{6}$$

where $\tau_{int}(t)$ is the wind stress integrated from $t' = t_0$ to $t' = t$. It is the integral in the above equation that causes deviations from the power law and, as such, we will refer to this as the "correction" term. For an infinitesimally short wind event, $\tau_{int}(t)$ is given by a step function (figure 7). This means the integrand in equation 6 will only be non-zero at times following the wind event. Evaluating equation 6 for an infinitesimally short wind event we recover equation 5 exactly.

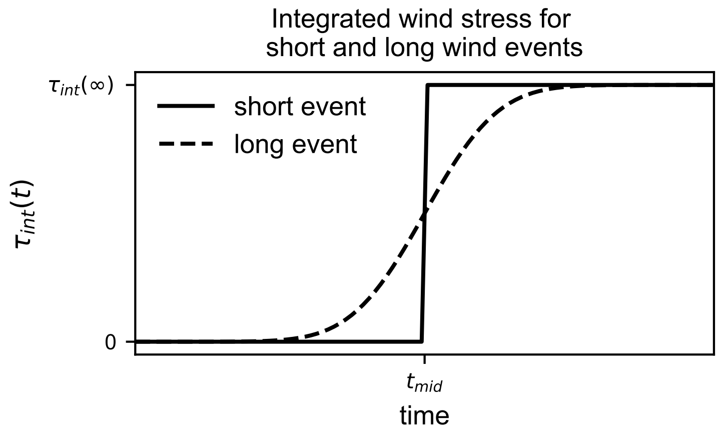

Figure 7. Integrated wind stress as a function of time for wind events with short and long durations. For short wind events (solid line) the wind stress resembles a step function, whereas for longer wind events (dashed line) the integrated wind stress varies more gradually.

For a longer wind event, $\tau_{int}(t)$ increases more gradually (figure 7), meaning that the integrand is non-zero over a wider time interval. This means that, for a given wind strength, the "correction" term is larger, leading to larger deviations from the power law. Because of this, care should be taken when considering whether the power law scaling applies to longer or stronger wind events than those discussed here.

4.2 Water mass transformation

The water mass transformation framework of Walin (1982) allows us to quantify diapycnal volume fluxes (which represent the amount of diapycnal mixing) integrated along isopycnals. Consider a volume of size ΔV bounded above and below by isopycnals of density σ and $\sigma+\Delta\sigma$ respectively. In a closed domain, the only way the volume between the isopycnals can change is if there is a convergence or divergence of the diapycnal volume fluxes, G, integrated over the isopycnals. This quantity is often referred to as the water mass transformation rate. Mathematically we can write

$$\frac{\partial \Delta V}{\partial t} = G(\sigma) - G(\sigma + \Delta\sigma)\,, \tag{7}$$

with positive values of G indicating a flux from lighter to denser water. The time mean fluxes, G, can be diagnosed from the instantaneous density field as follows:

1. define density bins, and at the first and last time-step, bin grid cell volumes by their instantaneous density. Sum all the volumes in the bin to find $\Delta V(\sigma, t)$;
2. subtract these values and divide by the elapsed time to find the time averaged value of $\partial_t \Delta V(\sigma)$;
3. cumulatively integrate the time averaged value of $\partial_t \Delta V(\sigma)$ over density, with the boundary condition of $G(\sigma_{max}) = 0$.

Thus we are able to find the time averaged $G(\sigma)$.

Figure 8a shows the time averaged water mass transformation rates in density space for the standard three-dimensional (blue) and two-dimensional integrations (orange), and the coarse two-dimensional control integration (green). The grey envelope displays the maximum and minimum transformation from the 2D ensemble of simulations. The coarse

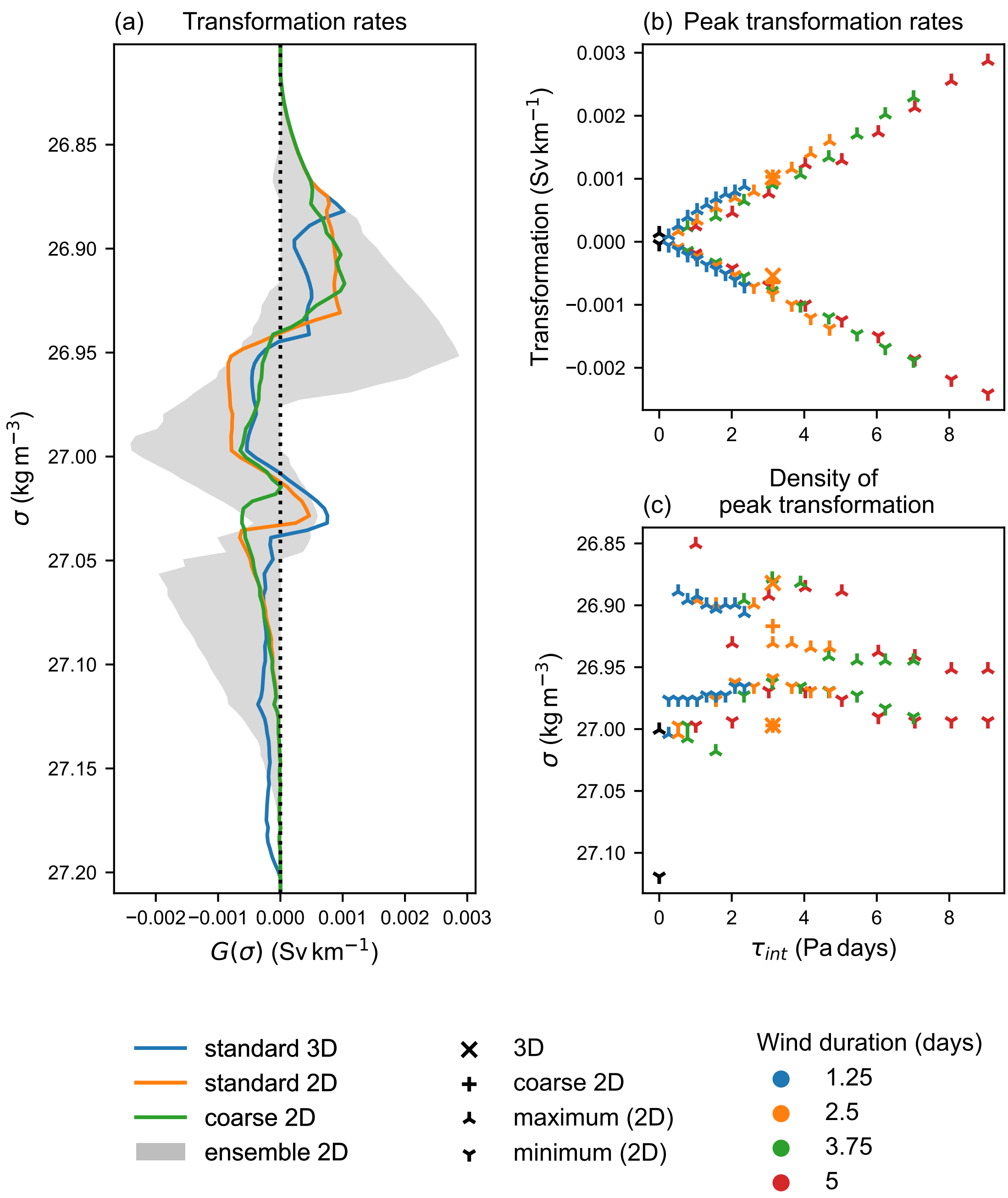

Figure 8. (a) Water mass transformation rates for the standard 3D (blue), standard 2D (orange) and coarse 2D (green) integrations. Grey envelope denotes the maximum and minimum transformation rates across the 2D ensemble. The plotted rates have the dimensions of transformation per unit length. To get the transformation in Sv the data should be multiplied by the length of the current, which for the East Greenland Current system is around 200 km. (b) The maximum (upward pointing triagonals) and minimum (downward pointing triagonals) water mass transformation rates as a function of integrated wind stress. (c) The densities of the maximum (upward pointing triagonals) and minimum (downward pointing triagonals) water mass transformation rates as a function of integrated wind stress. In panels (b) and (c) colour corresponds to the duration of the wind event. In place of triagonals, the standard 3D model is represented by a cross and the coarse 2D model is represented by a plus.

two-dimensional model (green) does a good job of representing the transformation close to the surface relative to its finer resolution counterpart (orange); however, transformation is suppressed at depth — in particular in the 27.00 $\mathrm{kg\,m^{-3}}$ to 27.05 $\mathrm{kg\,m^{-3}}$ density classes. This suggests that transformation rates in the standard 3D model are likely reasonable and possibly slightly underestimated.

The transformation rates have a double peak structure, with two maxima and two minima as a function of depth. Broadly speaking this means we have two density classes at which the transformation rates converge (are formed) and three density classes at which the transformation rates diverge (water masses are depleted). For the model integrations plotted, the lightest water mass formed has a density of between 26.90 $\mathrm{kg\,m^{-3}}$ and 26.95 $\mathrm{kg\,m^{-3}}$ with a deeper set of water masses formed between around 27.00 $\mathrm{kg\,m^{-3}}$ and 27.05 $\mathrm{kg\,m^{-3}}$. Waters with density between these two classes are depleted as are surface and deep waters. All models with non-negligible transformation rates have double transformation peaks. The lighter of these water mass classes corresponds to water masses in the core of the East Greenland Coastal Current between depths of 100 m and 200 m; whereas, the heavier water mass class corresponds to water masses in the core of the East Greenland-Irminger Current in the same depth range.

Comparing the standard two-dimensional (orange) and three-dimensional (blue) models, we see that baroclinic instability suppresses water mass transformation near the surface, especially in the 26.90 $\mathrm{kg\,m^{-3}}$ to 26.95 $\mathrm{kg\,m^{-3}}$ class. This is likely a result of the restratifying effect of the baroclinic instability. In the 27.00 $\mathrm{kg\,m^{-3}}$ to 27.05 $\mathrm{kg\,m^{-3}}$ density range there is enhanced downwelling. This corresponds to the density classes present on the inner shelf of the model, where we see enhanced restratification in the three-dimensional model (see figure 5 for example).

Figure 8b shows how the maximum and minimum of the time averaged diapycnal volume fluxes vary with the integrated wind stress — the response is linear. The rates have both maxima and minima as at different depths the diapycnal volume flux may be towards either lighter or denser waters. Also shown on this panel are transformation rates from the coarse and three-dimensional models, which appear to follow the same relationship as the two-dimensional ones. Performing a linear regression over data points from the two-dimensional ensemble, and using a t-test to find the confidence intervals, we find that the maximum and minimum transformation rates scale as $(3.00\pm0.20)\times10^{-4}$ $\mathrm{Sv\,km^{-1}\,Pa^{-1}\,day^{-1}}$ and $(-2.69 \pm 0.08) \times 10^{-4}$ $\mathrm{Sv\,km^{-1}\,Pa^{-1}\,day^{-1}}$, respectively.

Figure 8c shows how the isopycnals of maximum and minimum transformation vary with the wind stress. Above a wind stress of approximately 3 Pa days, the isopycnals are unaffected by the integrated wind stress, with maximal densification close to the surface and the lightening of deeper waters. The maxima and minima sit directly above and below the lighter of the two water mass classes that are formed, meaning transformation between the upper water masses is greatest.

Given the linearity of the peak transformation rates with respect to the integrated wind stress (figure 8a), we can estimate an upper bound on the average transformation rate over the course of a season. The average transformation rate will be given by the scaling of the peak transformation rate multiplied by the down-front wind stress integrated over a season. This is an upper bound on the mixing as we expect the mixing rates to saturate as we go to larger wind stresses (in a similar way to how the changes in mixed layer depth saturate). Using ERA5 hourly data (Hersbach et al., 2020; Copernicus Climate Change Service, 2023) we calculate the zonal average of the meridional wind stress at 60°N between 43°W and 41°W for the months of November through April, from 2014 to 2018. We select observations with southerly wind stresses and integrate the resulting time series over the time dimension. We get a wintertime total integrated down-front wind stress of 30 Pa days. Assuming a current length of 200 km and a scaling of 3×10^{-4} $\mathrm{Sv\,km^{-1}\,Pa^{-1}\,day^{-1}}$ (as previously calculated) we get a transformation rate of 1.8 Sv at $\sigma \approx 26.95$ $\mathrm{kg\,m^{-3}}$.

For a given wind duration, there will be a wind stress at which increasing the integrated wind stress does not lead to an increase in mixing — the linear relationship between water mass transformation rates and integrated wind stress will break down. Wind stresses over this threshold will cause the same amount of mixing as if the wind stress were *at* this threshold and so 1.8 Sv of water mass transformation will be an upper bound on the amount of mixing occurring in winter. We now attempt to estimate the wintertime mean transformation rate as a function of the wind stress at which the linear relationship breaks down — the saturation wind stress. We calculate the wintertime mean integrated wind stress from the same ERA5 data as used above; however, we set any wind stresses above a critical value, τ_{crit}, to be equal to τ_{crit}. We do this for a range of values of τ_{crit} and obtain the curve shown in figure 9. Given that in this study we tested wind stresses degree of confidence that we expect winter time wind events to produce *at least* 1.5 Sv of extra transformation across $\sigma \approx 26.95\ \mathrm{kg\,m^{-3}}$ (this is the amount of transformation that occurs with a saturation wind stress of $0.75\ \mathrm{N\,m^{-2}}$.)

The scaling used in estimating this seasonal range corresponds to peak transformation rates, which as we have just seen, describes the transformation of surface waters into "East Greenland Coastal Current waters". There will also be weaker transformation between denser water classes, and as figure 8a shows, the order of magnitude will likely be similar.

In summary we expect down-front wind events to drive between 1.5 Sv and 1.8 Sv of water mass transformation during wintertime. This suggests that down-front wind events may be one mechanism by which water is preconditioned to form North Atlantic Deep Waters in the sub-polar North Atlantic during wintertime. Furthermore, the changes in mixed layer depth following the down-front wind events imply that symmetric and baroclinic instabilities are key processes in setting the stratification off the coast of Greenland. During summertime the down-front wind events tend to be less intense with the integrated wind stress summing to 16 Pa days, implying transformation rates are roughly halved at this time of year.

5 Discussion

Of key concern to those running, or using output from, numerical ocean models is how well the model in question captures these down-front wind events and whether they should be parameterised. This of course depends on the specific model configuration in question; however, we would like to make the following general remarks. If the model is not eddy resolving, it will certainly not be resolving symmetric instability. Attempting to parameterise the process is likely a waste of time as the areas where the parameterisation is active will be a few grid cells thick at most and much bigger biases will likely be introduced by the lack of eddies in the model.

If, however, the model is eddy permitting or eddy resolving, a submesoscale parameterisation would likely improve the representation of these down-front wind events. The parameterisation of Bachman et al. (2017) may be effective — the parameterisation makes use of the scaling proposed by Taylor and Ferrari (2010) which we showed here to be a good fit to our models. Comparing results from our models with a coarse resolution parameterised model is a clear next step in ascertaining whether parameterisations can adequately represent the submesoscale response to down-front wind events. If a good parameterisation for the dynamics can be identified, it will become possible to examine the effect of down-front wind events over longer spatial and temporal scales. This will enable independent estimates of the amount of wintertime mixing induced by down-front wind events in the Sub-polar North Atlantic.

Large changes in the depth of the mixed layer following the excitement of symmetric instability imply that the instability is a key process in setting the vertical stratifi-

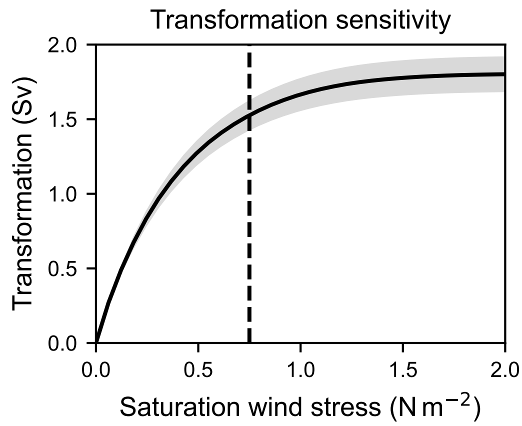

Figure 9. Wintertime transformation plotted as a function of the wind stress at which water mass transformation rates saturate. The true saturation wind stress in unknown; however, the dashed line shows the wind stress at 0.75 N m^{-2}, which puts a lower bound on the saturation wind stress. As such, it is likely that the true wintertime transformation rate into "East Greenland Coastal Current waters" at $\sigma \approx 26.95$ kg m^{-3} lies somewhere in the range 1.5 Sv to 1.8 Sv. Shading shows the range of the transformation when calculated using the 95% confidence intervals on the transformation rate scaling factors previously calculated. We assume a current length of 200 km.

cation in the western boundary region of the Irminger Sea. The water mass transformation rates, however, show that this mixing occurs mostly within lighter surface waters, and does not lead to the direct formation of North Atlantic Deep Waters. It may be tempting to use this as evidence that the action of the instability can be neglected but this is a simplistic interpretation of the results. Surface waters must lose a lot of buoyancy on their journey to the deep ocean, and symmetric instability may be one of several mechanisms that lowers it. Symmetric instability may then act to precondition surface waters before their subsequent transformation into deep waters.

This study didn't examine the role of down-front wind events in the lateral transport of fresh water and heat; however, given the intense eddy field and overturning cells that develop during these wind events, it seems plausible that the events could be responsible for large fluxes of salt away from the coast of Greenland and into the ocean interior. Further research is required to estimate the magnitude of these fluxes. If they are found to be significant, there would be an extra impetus to go to the expense of parameterising the submesoscale instabilities excited during down-front wind events.

6 Conclusions

Observations show that strong northerly winds during spring and winter trigger the excitement of Ekman induced symmetric instability in the western boundary region of the Irminger Sea (Le Bras et al., 2022). This leads to the development of a deep low potential vorticity layer that sits below the conventionally defined convectively mixed layer (Le Bras et al., 2022; Taylor & Ferrari, 2010). The spatial sparsity of existing moored observations makes it difficult to determine the spatial structure of mixing and mixing rates during these wind events.

We have used an idealised two-dimensional model with resolution of 25 m and an idealised three-dimensional model with a resolution of 200 m to investigate how down-front wind events alter the stratification in the region. The two-dimensional model allowed the development of symmetric instability only, whereas the three-dimensional model allowed the development of both symmetric and baroclinic instabilities. The models were forced with a spatially constant but temporally varying wind stress. We found that in both models, over short time scales symmetric and gravitational instability are the dominant processes. A deep low potential vorticity layer which is almost indistinguishable from, but deeper than, the convectively mixed layer develops in both models. In the three-dimensional model, we see restratification at the surface of the low potential vorticity layer through the action of baroclinic instability following the down-front wind event. We propose that the short time scale response (up to two weeks) of the flow to down-front wind forcing is gravitational instability, with symmetric instability dominating over intermediate time scales (two to four weeks) and baroclinic instability dominating over longer timescales (over four weeks.)

In order to investigate how the duration and strength of wind events influence diapycnal mixing, we integrated an ensemble of two-dimensional models with different wind forcing. We defined the quantity the integrated wind stress and hypothesised that the depth of the low potential vorticity layer following down-front wind events varies according to its square root. The low potential vorticity layer scaling within the model ensemble was consistent with this prediction; however, we also found that the duration of wind events limits the deepening of the mixed layer. This suggests mixing rates saturate when the wind stress is sufficiently large.

We calculated time mean water mass transformation rates for our ensemble and found that the maximum and minimum rates scale linearly with the integrated wind stress. Using ERA5 reanalysis data (Hersbach et al., 2020) and the linear relationship between integrated wind stress and water mass transformation rates, we estimated the mean wintertime water mass transformation rate to be 1.8 Sv. This calculation assumes there is no saturation in transformation rates at high wind stresses. Taking into account the saturation of water mass transformation rates when wind stresses are large, we estimate between 1.5 Sv and 1.8 Sv of water mass transformation are produced by down-front wind events each winter. This transformation is between light surface waters and East Greenland Coastal Current waters; however, there will also be formation of East Greenland-Irminger Current waters at a similar but slightly lower rate.

Coarse resolution numerical ocean models do not resolve symmetric instability. We suggest that models that do not resolve mesoscale eddies should not worry about this omission as the absence of eddies is likely leading to much larger biases. Eddy permitting and eddy resolving models should, however, consider parameterising the response of the ocean to down-front wind events, as failing to do so will lead to biases in the stratification. In particular the surface may end up overly stratified following down-front wind events. We suggest the parameterisation of Bachman et al. (2017) may capture the dynamics well as it uses the scaling of Taylor and Ferrari (2010) which, as we have demonstrated, is effective at predicting mixed layer depths in the idealised models presented here. Future work should ascertain whether this is indeed the case.

This work has focused on diapycnal transports following down-front wind events. We have not investigated along-isopycnal transports of heat and salt, partly due to the single buoyancy tracer employed by our models making them ill suited for such studies. This is, however, a clear avenue for future research. Waters off the coast of Greenland are salinity stratified whereas in the interior of the Irminger Sea they are thermally stratified (Le Bras et al., 2022). Both symmetric instability and baroclinic eddies are effective at producing along-isopycnal mixing (Abernathey et al., 2022) and may be responsible for significant diahaline and diathermal transports, fluxing heat and salt between the boundary and the interior of the Irminger Sea.

Open Research Section

All processed data and a selection of the raw data used in this study is available at `https://dx.doi.org/doi:10.5281/zenodo.8232682` (F. Goldsworth et al., 2023). Code used for model integrations and subsequent analysis is available at `https://dx.doi.org/doi:10.5281/zenodo.8233578` (F. Goldsworth, 2023).

Acknowledgments

We are grateful for the financial support of the Natural Environment Research Council (grants NE/L002612/1 and NE/T013494/1). This work used the ARCHER2 UK National Supercomputing Service (`https://www.archer2.ac.uk`). We would also like to thank Andrew Coward for providing computational support. The results contain modified Copernicus Climate Change Service information 2020. Neither the European Commission nor ECMWF is responsible for any use that may be made of the Copernicus information or data it contains.

References

Abernathey, R., Gnanadesikan, A., Pradal, M.-A., & Sundermeyer, M. A. (2022, January). Chapter 9 - Isopycnal mixing. In M. Meredith & A. Naveira Garabato (Eds.), *Ocean Mixing* (pp. 215–256). Elsevier. doi: 10.1016/B978-0-12-821512-8.00016-5

Allen, J. S., & Newberger, P. A. (1996, October). Downwelling circulation on the Oregon Continental Shelf. Part I: Response to idealized forcing. *Journal of Physical Oceanography*, *26*(10), 2011–2035. doi: 10.1175/1520-0485(1996)026⟨2011:DCOTOC⟩2.0.CO;2

Bachman, S. D., Fox-Kemper, B., Taylor, J. R., & Thomas, L. N. (2017). Parameterization of frontal symmetric instabilities. I: Theory for resolved fronts. *Ocean Modelling*, *109*, 72–95. doi: 10.1016/j.ocemod.2016.12.003

Broecker, W. S. (1991). The Great Ocean Conveyor. *Oceanography*, *4*(2), 79–89.

Campin, J.-M., Heimbach, P., Losch, M., Forget, G., edhill3, Adcroft, A., ... Deremble, B. (2022, April). *MITgcm/MITgcm: checkpoint68i* [Software]. zenodo. doi: 10.5281/zenodo.6498956

Clément, L., Frajka-Williams, E., Von Oppeln-Bronikowski, N., Goszczko, I., & De Young, B. (2023, May). Cessation of Labrador Sea convection triggered by distinct fresh and warm (sub)mesoscale flows. *Journal of Physical Oceanography*. doi: 10.1175/JPO-D-22-0178.1

Copernicus Climate Change Service. (2023). *ERA5 hourly data on single levels from 1940 to present* [Dataset]. Copernicus Climate Change Service (C3S) Climate Data Store (CDS). doi: 10.24381/cds.adbb2d47

Daniault, N., Mercier, H., & Lherminier, P. (2011, April). The 1992-2009 transport variability of the East Greenland-Irminger Current at 60°N. *Geophysical Research Letters*, *38*(7), n/a-n/a. doi: 10.1029/2011GL046863

D'Asaro, E., Lee, C., Rainville, L., Harcourt, R., & Thomas, L. N. (2011). Enhanced turbulence and energy dissipation at ocean fronts. *Science*, *332*(6027), 318–322. doi: 10.1126/science.1201515

de Jong, M. F., & de Steur, L. (2016). Strong winter cooling over the Irminger Sea in winter 2014–2015, exceptional deep convection, and the emergence of anomalously low SST. *Geophysical Research Letters*, *43*(13), 7106–7113. doi: 10.1002/2016GL069596

Emanuel, K. A. (1994). Slantwise convection. In *Atmospheric Convection* (pp. 392–417). Oxford: Oxford University Press.

Ertel, H. (1942, September). Ein neuer hydrodynamischer Erhaltungssatz. *Naturwissenschaften*, *30*(36), 543–544. doi: 10.1007/BF01475602

GEBCO Compilation Group. (2020). *GEBCO 2020 grid* [Dataset]. doi: 10.5285/a29c5465-b138-234d-e053-6c86abc040b9

Goldsworth, F. (2023, August). *fraserwg/irminger-proj: v1.1* [Software]. Zenodo. doi: 10.5281/zenodo.8233578

Goldsworth, F., Le Bras, I., Johnson, H., & Marshall, D. (2023, August). *Data for "Saturation of destratifying and restratifying instabilities during down front wind events: A case study in the Irminger Sea"* [Dataset]. Zenodo. doi: 10.5281/zenodo.8232682

Goldsworth, F. W. (2022). *Symmetric instability in the Atlantic Meridional Overturning Circulation* (Doctoral dissertation, University of Oxford, Oxford). doi: 10.5287/ora-xogpmrvzd

Griffies, S. M., & Hallberg, R. W. (2000, August). Biharmonic friction with a Smagorinsky-like viscosity for use in large-scale eddy-permitting ocean models. *Monthly Weather Review*, *128*(8), 2935–2946. doi: 10.1175/1520-0493(2000)128⟨2935:bfwasl⟩2.0.co;2

Griffiths, S. D. (2003). Nonlinear vertical scale selection in equatorial inertial instability. *Journal of the Atmospheric Sciences*, *60*(7), 977–990. doi: 10.1175/1520-0469(2003)060⟨0977:NVSSIE⟩2.0.CO;2

Haine, T. W. N., & Marshall, J. (1998, April). Gravitational, symmetric, and baroclinic instability of the ocean mixed layer. *Journal of Physical Oceanography*, *28*(4), 634–658. doi: 10.1175/1520-0485(1998)028⟨0634:gsabio⟩2.0.co;2

Hersbach, H., Bell, B., Berrisford, P., Hirahara, S., Horányi, A., Muñoz-Sabater, J., ... Thépaut, J.-N. (2020, July). The ERA5 global reanalysis. *Quarterly Journal of the Royal Meteorological Society*, *146*(730), 1999–2049. doi: 10.1002/qj.3803

Hirschi, J. J., Barnier, B., Böning, C., Biastoch, A., Blaker, A. T., Coward, A., ... Xu, X. (2020). The Atlantic Meridional Overturning Circulation in high-resolution models. *Journal of Geophysical Research: Oceans*, *125*(4), 1–35. doi: 10.1029/2019JC015522

Hoskins, B. J. (1974, July). The role of potential vorticity in symmetric stability and instability. *Quarterly Journal of the Royal Meteorological Society*, *100*(425), 480–482. doi: 10.1002/qj.49710042520

Josey, S. A., de Jong, M. F., Oltmanns, M., Moore, G. K., & Weller, R. A. (2019). Extreme variability in Irminger Sea winter heat loss revealed by Ocean Observatories Initiative mooring and the ERA5 reanalysis. *Geophysical Research Letters*, *46*(1), 293–302. doi: 10.1029/2018GL080956

Le Bras, I. A.-A., Callies, J., Straneo, F., Biló, T. C., Holte, J., & Johnson, H. L. (2022, October). Slantwise convection in the Irminger Sea. *Journal of Geophysical Research: Oceans*, *127*(10). doi: 10.1029/2022JC019071

Le Bras, I. A.-A., Straneo, F., Holte, J., & Holliday, N. P. (2018, December). Seasonality of freshwater in the East Greenland Current System from 2014 to 2016. *Journal of Geophysical Research: Oceans*, *123*(12), 8828–8848. doi: 10.1029/2018JC014511

Lozier, M. S., Li, F., Bacon, S., Bahr, F., Bower, A. S., Cunningham, S. A., ... Zhao, J. (2019, February). A sea change in our view of overturning in the subpolar North Atlantic. *Science*, *363*(6426), 516–521. doi: 10.1126/science.aau6592

Marshall, J., Adcroft, A., Hill, C., Perelman, L., & Heisey, C. (1997). A finite-volume, incompressible navier stokes model for, studies of the ocean on parallel computers. *Journal of Geophysical Research: Oceans*, *102*(C3), 5753–5766. doi: 10.1029/96JC02775

Plougonven, R., & Zeitlin, V. (2009). Nonlinear development of inertial instability in a barotropic shear. *Physics of Fluids*, *21*(10). doi: 10.1063/1.3242283

Prather, M. J. (1986). Numerical advection by conservation of second-order moments. *Journal of Geophysical Research: Atmospheres*, *91*(D6), 6671. doi: 10

.1029/JD091iD06p06671

Shu, R. (2023, May). Slantwise convection in the West Greenland Current. In *21st Arctic-Subarctic Ocean Fluxes Workshop.* Gran Canaria.

Smagorinsky, J. (1963, March). General circulation experiments with the primitive equations. *Monthly Weather Review*, *91*(3), 99–164. doi: 10.1175/1520-0493(1963)091⟨0099:GCEWTP⟩2.3.CO;2

Spall, M. A., & Thomas, L. N. (2016, October). Downfront winds over buoyant coastal plumes. *Journal of Physical Oceanography*, *46*(10), 3139–3154. doi: 10.1175/JPO-D-16-0042.1

Stamper, M. A., & Taylor, J. R. (2017, January). The transition from symmetric to baroclinic instability in the Eady model. *Ocean Dynamics*, *67*(1), 65–80. doi: 10.1007/s10236-016-1011-6

Stone, P. H. (1966, July). On non-geostrophic baroclinic stability. *Journal of the Atmospheric Sciences*, *23*(4), 390–400. doi: 10.1175/1520-0469(1966)023⟨0390:ONGBS⟩2.0.CO;2

Straneo, F., Kawase, M., & Pickart, R. S. (2002). Effects of wind on convection in strongly and weakly baroclinic flows with application to the Labrador Sea. *Journal of Physical Oceanography*, *32*(9), 2603–2618. doi: 10.1175/1520-0485(2002)032⟨2603:EOWOCI⟩2.0.CO;2

Talley, L. D., Pickard, G. L., Emery, W. J., & Swift, J. H. (2011a, January). Chapter 12 - Arctic Ocean and Nordic Seas. In L. D. Talley, G. L. Pickard, W. J. Emery, & J. H. Swift (Eds.), *Descriptive Physical Oceanography (Sixth Edition)* (pp. 401–436). Boston: Academic Press. doi: 10.1016/B978-0-7506-4552-2.10012-5

Talley, L. D., Pickard, G. L., Emery, W. J., & Swift, J. H. (2011b, January). Chapter 9 - Atlantic Ocean. In L. D. Talley, G. L. Pickard, W. J. Emery, & J. H. Swift (Eds.), *Descriptive Physical Oceanography (Sixth Edition)* (pp. 245–301). Boston: Academic Press. doi: 10.1016/B978-0-7506-4552-2.10009-5

Taylor, J. R., Bachman, S., Stamper, M., Hosegood, P., Adams, K., Sallee, J.-B., & Torres, R. (2018, March). Submesoscale Rossby waves on the Antarctic Circumpolar Current. *Science Advances*, *4*(3), eaao2824. doi: 10.1126/sciadv.aao2824

Taylor, J. R., & Ferrari, R. (2009). On the equilibration of a symmetrically unstable front via a secondary shear instability. *Journal of Fluid Mechanics*, *622*, 103–113. doi: 10.1017/S0022112008005272

Taylor, J. R., & Ferrari, R. (2010, June). Buoyancy and wind-driven convection at mixed layer density fronts. *Journal of Physical Oceanography*, *40*(6), 1222–1242. doi: 10.1175/2010JPO4365.1

Thomas, L. N., & Lee, C. M. (2005). Intensification of ocean fronts by down-front winds. *Journal of Physical Oceanography*, *35*(6), 1086–1102. doi: 10.1175/JPO2737.1

Thomas, L. N., Taylor, J. R., Ferrari, R., & Joyce, T. M. (2013, July). Symmetric instability in the Gulf Stream. *Deep Sea Research Part II: Topical Studies in Oceanography*, *91*, 96–110. doi: 10.1016/j.dsr2.2013.02.025

Walin, G. (1982). On the relation between sea-surface heat flow and thermal circulation in the ocean. *Tellus*, *34*(2), 187–195. doi: 10.3402/tellusa.v34i2.10801

Yankovsky, E., & Legg, S. (2019). Symmetric and baroclinic instability in dense shelf overflows. *Journal of Physical Oceanography*, *49*(1), 39–61. doi: 10.1175/JPO-D-18-0072.1